Indium Gallium Oxide Alloys: Electronic Structure, Optical Gap, Surface Space Charge and Chemical Trends within Common Cation Semiconductors

Jack E. N. Swallow,[†,‡] Robert G. Palgrave,[¶] Philip A. E. Murgatroyd,[†] Anna Regoutz,[¶] Michael Lorenz,[§] Anna Hassa,[§] Marius Grundmann,[§] Holger von Wenckstern,[§] Joel B. Varley,[‖] and Tim D. Veal[*,†]

[†]*Stephenson Institute for Renewable Energy and Department of Physics, University of Liverpool, Liverpool L69 7ZF, U.K.*

[‡]*Department of Materials, University of Oxford, Parks Road, Oxford OX1 3PH, U.K.*

[¶]*Department of Chemistry, University College London, 20 Gordon Street, London WC1H 0AJ, U.K.*

[§]*Felix Bloch Institute for Solid State Physics, Universität Leipzig, Leipzig, Germany*

[‖]*Lawrence Livermore National Laboratory, Livermore, California 94550, USA*

E-mail: t.veal@liverpool.ac.uk

Abstract

The electronic and optical properties of $(In_xGa_{1-x})_2O_3$ alloys are highly tunable, giving rise to a myriad of applications including transparent conductors, transparent electronics and solar-blind ultraviolet photodetectors. Here, we investigate these properties for a high quality pulsed laser deposited film which possesses a lateral cation composition gradient ($0.01 \leq x \leq 0.82$) and three crystallographic phases (monoclinic, hexagonal and bixbyite). The optical gaps over this composition range are determined and only a weak optical gap bowing is found ($b = 0.36$ eV). The valence band edge evolution along with the change in the fundamental band gap over the composition gradient enables the surface space-charge properties to be probed. This is an important property when considering metal contact formation and heterojunctions for devices. A transition from surface electron accumulation to depletion occurs at $x \sim 0.35$ as the film goes from the bixbyite In_2O_3 phase to the monoclinic β-Ga_2O_3 phase. The electronic structure of the different phases is investigated using density functional theory calculations, and compared to the valence band X-ray photoemission spectra. Finally, the properties of these alloys, such as the n-type dopability of In_2O_3 and use of Ga_2O_3 as a solar-blind UV detector, are understood with respect to other common-cation compound semiconductors in terms of simple chemical trends of the band edge positions and the hydrostatic volume deformation potential.

Keywords

Indium Oxide, Gallium Oxide, Indium Gallium Oxide, XPS, Chemical Trends

1 Introduction

Indium oxide (In_2O_3) is the material of choice (most often doped with Sn) for applications requiring transparent conductive electrodes, owing to its propensity for n-type dopability providing great electrical performance, and its large energy gap ($\sim$2.9 eV fundamental band gap and $\sim$3.7 eV for the first dipole-allowed transition[1]) giving high optical transparency.[2] In contrast, β-gallium oxide (β-Ga_2O_3) is a rapidly emerging semiconductor material and its fundamental properties have been relatively less explored in comparison. With a high breakdown voltage and very large optical gap ($\sim$4.8 eV), β-Ga_2O_3 is a promising candidate for applications in high-power electronic devices and solar-blind UV detectors.[3] Indium gallium oxide alloys have generated much research interest in the past, often in the amorphous state used for thin film transistors.[4–7]

Favourable energy alignment when forming heterojunctions and alloys is imperative for optimal device performance. Hence, careful engineering of the optical gap and surface electronic properties of In_2O_3 and β-Ga_2O_3 would bring a multitude of new potential applications. Fortunately, alloys formed from In_2O_3 and β-Ga_2O_3 possess the potential for such desirable properties and tunability due to the large band gap disparity and different surface space-charge behaviour. The potential for band gap tailoring as well as control of the surface space-charge is therefore a very exciting prospect for indium gallium oxide ((In_xGa_{1-x})$_2O_3$) alloys. However, In_2O_3 and β-Ga_2O_3 possess very different crystal structures as presented in Figure 1. β-Ga_2O_3 has a monoclinic structure with two inequivalent Ga sites, a distorted tetrahedral site and a distorted octahedral site (Figure 1(a)). In_2O_3 has a cubic (bixbyite) unit cell also with two inequivalent cation sites, a distorted and a symmetric octahedron (Figure 1(c)). Further, an intermediate hexagonal $InGaO_3$ phase has been reported, which has a symmetric In site and a trigonal bipyramidal Ga site (Figure 1(b)).[8–10] It is not yet well explored how these different structures affect the surface electronic properties of these materials. This fundamental understanding is of great importance for the development of new electronic devices and heterostructures. Recent developments in deposition methods

and combinatorial material science (materials possessing a composition gradient)[8] give us the ability to quickly and rigorously determine the properties of many new material compositions using one film.
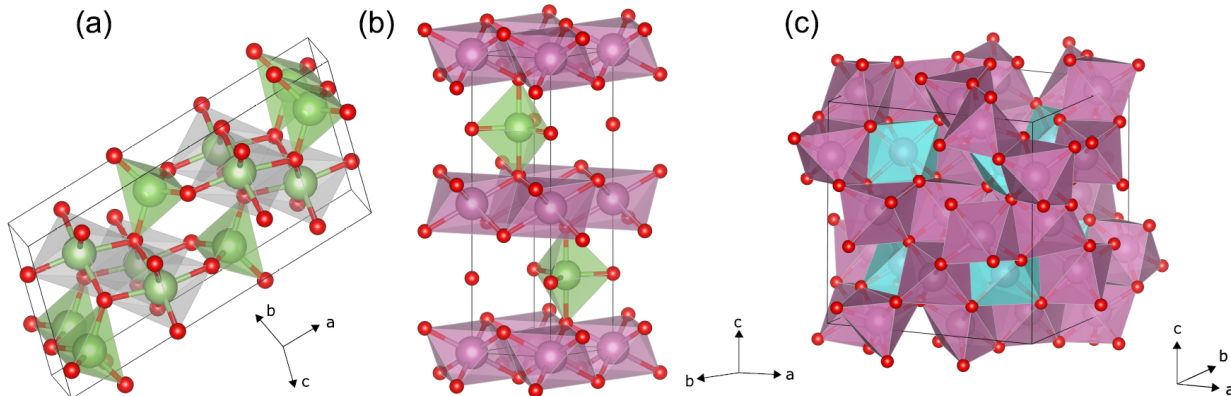

Figure 1: Unit cells of (a) monoclinic β-Ga_2O_3, (b) hexagonal phase $InGaO_3$ and (c) bixbyite In_2O_3. Ga atoms are shown in green, In atoms in purple and O atoms in red. For (a) and (c), the inequivalent cation sites are shown with different colour octahedra.

In this study, we employ the recent advances in high quality combinatorial growth methods with the rapid development in combinatorial measurement, in order to fully investigate the electronic structure and behaviour of $(In_xGa_{1-x})_2O_3$ alloys. We use high-resolution scanning X-ray photoemission spectroscopy (XPS), as well as state-of-the-art first-principles calculations to determine the electronic structure of $(In_xGa_{1-x})_2O_3$ combinatorial films over nearly the whole composition range ($0.01 < x < 0.82$). This combined with optical measurements help us to understand the compositional dependence of the Fermi level with respect to the band edges at the surface of $(In_xGa_{1-x})_2O_3$. We explore the surface space-charge transition from electron accumulation in In_2O_3 to depletion in β-Ga_2O_3, a property that has implications for the incorporation of these materials in devices in the future. We compare density functional theory (DFT) calculated density-of-states (DOS) for the different phases looking at the constituent orbital contributions, and also compare this to the XPS valence band spectra and occupied semi-core d levels. From this we observe indicators of p-d repulsion which affects the position of the VBM, as well as s-d hybridisation in the semi-core

4

levels which is associated with materials with similar energy s and d levels and occupied cation d levels. Looking at these orbital contributions, as well as knowledge of the volume deformation potential (how the material's band gap varies with changing volume), allows us to fully explore the chemical trends of In_2O_3 and β-Ga_2O_3. This explains why In_2O_3 is extremely n-type dopable, and why β-Ga_2O_3 has an extremely large band gap, even for an oxide semiconductor.

2 Methods

2.0.1 Experimental Details

A continuous composition spread (CCS) $(In_xGa_{1-x})_2O_3$ film was grown on a 51 mm-diameter c-plane sapphire wafer via pulsed laser deposition (PLD) using a two-fold azimuthally segmented target for ablation. SiO_2 (0.1 wt. %) was mixed with the In_2O_3 and Ga_2O_3 source powders prior to target fabrication, to achieve sufficient conductivity via Si n-type doping to avoid charging when performing XPS measurements. The growth temperature and oxygen background pressure were 650°C and 3×10^{-4} mbar, respectively. Further information on the deposition process is given by von Wenckstern *et al.*[8] A 4 mm-wide, 51 mm-long strip of the wafer with the full composition gradient across it was cut and all subsequent measurements were performed on this strip. The films surface roughness is not assessed here, but has been determined previously for this system deposited in the same way.[11] Despite an increase in surface roughness when the cubic bixbyite phase is reached, the films should have sufficiently low surface roughness required for device applications including heterostructure-based devices.

The spatial distribution of In, Ga and Si content throughout the film was determined by energy-dispersive X-ray spectroscopy (EDX) using an FEI NovaLab 200 equipped with an Ametek EDX detector. The spatially resolved X-ray diffraction patterns (XRD) from the film were recorded using a PANalytical X'pert PRO MRD X-ray diffractometer equipped with

a PIXcel3d detector operating in one-dimensional scanning mode with a monochromated Cu Kα source. The XPS measurements were performed using a Thermo Scientific K-Alpha instrument with a monochromated microfocused Al Kα X-ray source (1486.6 eV). These measurements were performed under ultrahigh vacuum (UHV) conditions ($<10^{-9}$ mbar). The scans were measured by focusing the beam width to 400 μm spot size on areas of the film with the film being translated by 1 mm between each measurement. An analyser pass energy of 50 eV was used, giving a spectrometer resolution of 0.65 eV, enabling peak positions to be determined to within ± 0.1 eV. Sample charging was corrected by a dual beam charge compensation system. Optical transmittance determination was performed using a Shimadzu UV-Vis-IR 3700 spectrophotometer with an integrating sphere detector which employs a photomultiplier detector to reach energies up to 6.5 eV. All measurements were performed at room temperature.

2.0.2 Computational Details

The theoretical calculations were performed using the HSE06 screened hybrid functional[12] and projector augmented wave (PAW) approach[13] as implemented in the VASP code.[14] We include semi-core $3d$ electrons of Ga and $4d$ electrons of In as explicit valence states and set the fraction of screened Hartree-Fock exchange to 32% for β-Ga$_2$O$_3$ and InGaO$_3$, and 28% for In$_2$O$_3$ (in order to better match the experimental band gaps). All unit cell parameters were optimized using a plane-wave cutoff of 520 eV and integrations over the Brillouin zone were performed using a 6×6×6 Γ-centered grid of Monkhorst-Pack special k-points for Ga$_2$O$_3$, a 10×10×4 grid for InGaO$_3$ and a 4×4×4 grid for In$_2$O$_3$. Densities of states were evaluated using the relaxed geometries and the tetrahedron method with Blöchl corrections[15] and included scalar-relativistic effects for the In-containing compounds.

For β-Ga$_2$O$_3$, this choice yields a direct band gap of 4.85 eV and optimal lattice constants of 12.21, 3.03, and 5.79 Å for the a, b, and c cell parameters, respectively, in excellent agreement with experimental values.[16–18] Our optimized lattice constants for the hexagonal

InGaO$_3$ phase were 3.31 and 12.03 Å for the a and c values, with a calculated direct band gap of 4.13 eV at the Γ-point. The indirect band gap was found to be lower, at 3.91 eV, with the valence band maximum falling nearly midway between the Γ and M points in the Brillouin zone. For cubic bixbyite In$_2$O$_3$, our optimized lattice constant was 10.12 Å, with a calculated direct band gap of 2.86 eV at the Γ-point.

3   Results and Discussion

3.0.1   Structure and Composition

Figure 2(a) shows a total of 45 single 2θ-ω XRD patterns that have been tessellated to form a false-colour plot, with lateral distance across the film on the y-axis and 2θ on the x-axis. Solid black lines have been superimposed on the pattern at around ∼6 mm and ∼9 mm and ∼40 mm to indicate the region of mainly the bixbyite phase (z≤7 mm), the onset of the InGaO$_3$ hexagonal (mixed) phase (∼7-12 mm) and the region of mostly monoclinic phase up until the end of the measurement region (∼50 mm). Figures 2(b-d) show single patterns corresponding to the top, middle and bottom solid lines. Figure 2(b) shows that the β-Ga$_2$O$_3$ phase is ($\bar{2}$01) oriented.[8,9,19] This holds true for the majority of the film. Figure 2(d) shows that the In$_2$O$_3$ dominated region of the film grows with (111) orientation, although a small peak just to the left of the 222 peak (∼29°) is also visible which originates from the 0004 reflection from the hexagonal InGaO$_3$ phase, consistent with figure 2(c).[8–10,19] In both plots we also see the 006 and 00 12 peaks due to the sapphire substrate, which have been left unlabelled. It is clear the (In$_x$Ga$_{1-x}$)$_2$O$_3$ material is crystalline across the whole film (and so the whole composition range).

We are able to directly quantify the spatial distribution of Ga, In and Si content of the film using EDX, and correlate these data with the XRD results by taking measurements at the same positions in the film, demonstrating the power of the combinatorial approach. Figure 3(a) displays an EDX line scan from 3 to 49 mm across the film. The Si content in
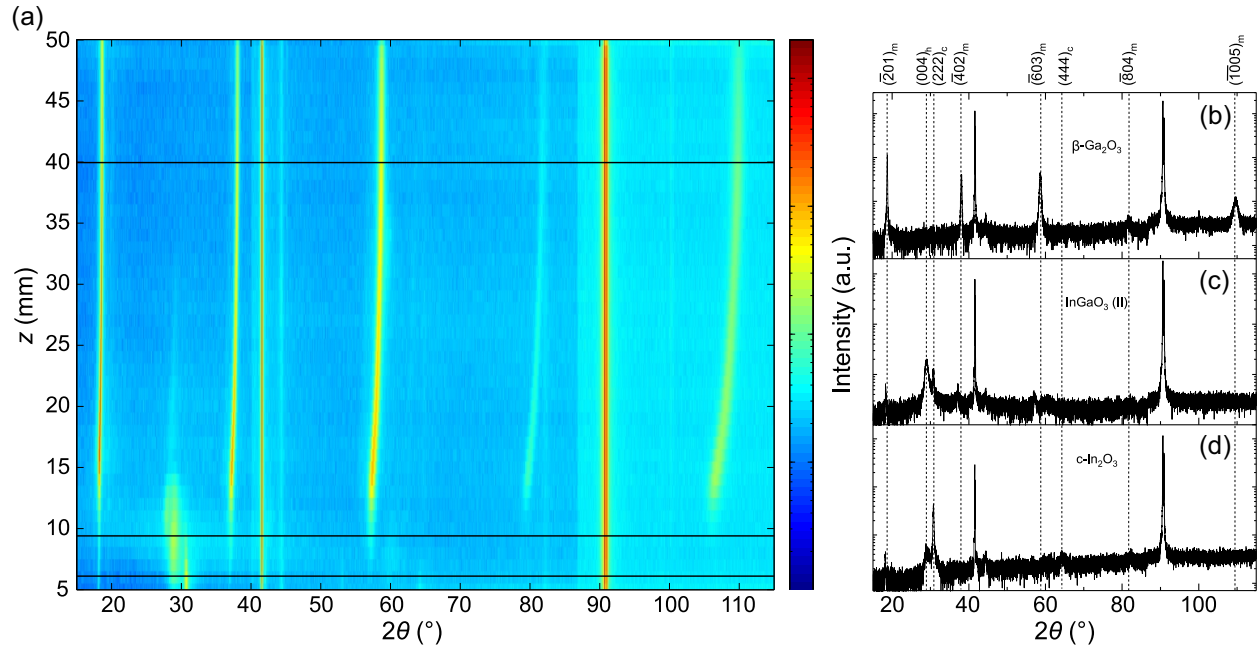
Figure 2: (a) False colour representation of wide-angle 2θ-ω XRD patterns, taken at $\sim$1 mm intervals (55 in total) across the compositionally graded strip in the direction highlighted by a black arrow in Figure 3. Black horizontal lines indicate: the point in the film corresponding to the monoclinic phase (top line), the onset of the hexagonal phase (middle line), and the onset of the bixbyite phase (bottom line). (b), (c) and (d) show individual diffraction patterns taken at the horizontal lines at 40, 9 and 6 mm, showing primarily (b) the monoclinic β-Ga_2O_3 phase, (c) the hexagonal $InGaO_3$ (II) and (d) the bixbyite In_2O_3 phase respectively. A small peak corresponding to the (0004) peak of the hexagonal $(In_xGa_{1-x})_2O_3$ phase can be seen at $\sim$29° in (d). Note the intensity scale in (b)-(d) is logarithmic.

the film varies minimally and it is ~ 0.6 at.% across the whole composition range.
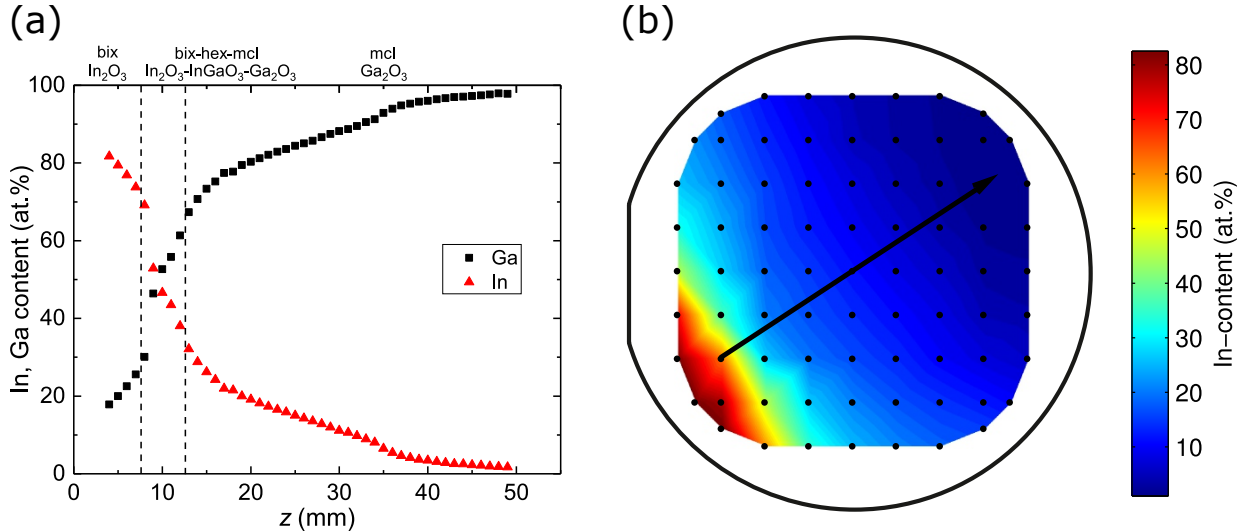

Figure 3: (a) EDX line scan of Ga and In content along the film. Black dashed lines represent positions of different crystallographic phases (bixbyite to mixed bixbyite-hexagonal-monoclinic to monoclinic). (b) EDX false colour map of In content in the as deposited $(In_xGa_{1-x})_2O_3$ film (51 mm diameter), the black arrow displaying the position where the line scan was taken, and a 4 mm wide strip was cut for further experiments.

There exists a mirror relationship between Ga and In content from z = 0 to z = 46 mm, i.e. as Ga content increases, In content decreases by the same amount. This reflects the substitution of Ga for In atoms in the unit cell. Dashed black lines are used to indicate the position in the film where a phase transition occurs in the XRD pattern presented in Figure 2. Between z = 0 and z = 5 mm, the In (Ga) content slowly decreases (increases). Past z = 5 mm, there is a rapid reduction (increase) in In (Ga) content. This is a common feature for combinatorial $(In,Ga)_2O_3$ thin films[9,19,20] deposited under oxygen-poor conditions, as detailed in Ref. 21. The hexagonal $InGaO_3$ phase is seen in the XRD regardless of the substrate chosen. Between z = 5 mm and z = 10 mm, there is a steep decrease (increase) in In (Ga) content which coincides with the phase change from bixbyite to hexagonal (mixed) phase. The atomic concentration of the mixed hexagonal phase is around $\sim$ 40–60 at.%, which correlates well with the expected ratios of In to Ga in the hexagonal $InGaO_3$ structure (roughly one to one In to Ga ratio). Beyond z = 10 mm, the rate of change of In/Ga content

across the film lessens, whilst the film takes on the monoclinic β-Ga_2O_3 structure. The false-colour plot of In content seen in Figure 3(b) shows this well with a very gradual growth of In content from right to left, until around a third of the distance along the film, when the In content increases rapidly. We also see the great control of In content over the film from the CCS PLD deposition method. The In content varies horizontally across the film but there is negligible variation vertically in the narrow strip of material investigated using photoemission spectroscopy.

3.0.2 Valence Band X-ray Photoelectron Spectroscopy

XPS is an extremely powerful tool for probing the electronic structure of materials. It is made even more informative when used as a combinatorial characterization method. Figure 4 shows the XPS valence band (VB) spectra of the material, with the leading edge enlarged in the right hand panel. The top-most data set, which is coloured in red, is taken from the Ga-rich end of the film, with subsequent spectra fading to black as more In content is incorporated. This is supported by the XPS peak intensities in SI Figure S1 where the Ga $2p$ peaks slowly diminish in intensity, while the In $3d$ intensity grows relatively moving down the plot. A very clear change in shape of the valence band can be seen in Figure 4, going from the broad β-Ga_2O_3 valence spectra to the narrower In_2O_3 spectra. This directly reflects the changes in structure seen in Figure 2. There is also a larger valence band maximum (VBM) to Fermi level (E_F) separation for β-Ga_2O_3 than for In_2O_3 (Ref. 22) as is clearly seen in Figure 4, as the VBM slowly moves from left to right as the In content increases.

The VBM position from each spectrum could be estimated by a linear extrapolation method to the leading edge of the valence spectra. However, due to the effects of instrumental broadening of the spectra, this is not an accurate method for determining the VBM position, especially for systems with a very high DOS at the VBM such as the flat bands of In_2O_3 and β-Ga_2O_3. Instead it is best practice to fit DFT-calculated valence spectra to the data and determine the energy distance from zero. This particular case is complicated further
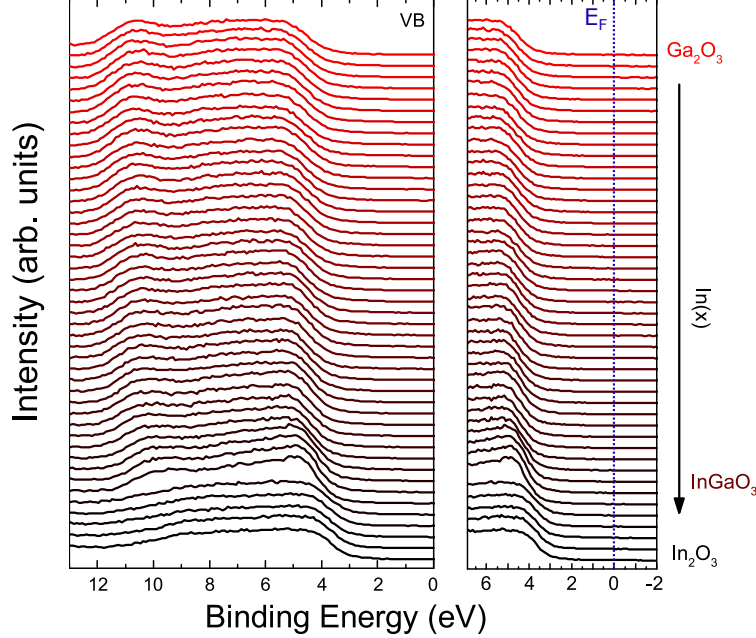
Figure 4: High resolution XPS plots of the valence band of $(In_xGa_{1-x})_2O_3$ film. 46 spectra were recorded across the film at 1 mm intervals, matching the EDX measurement in Figure 3. The spectra recorded from the Ga-rich end of the film are at the top, with increasing In content down the plot.

by the fact that we have many phases contributing to our spectra, making true calculated representation of the spectra very difficult (many calculations would be required). Instead, we acknowledge a $\sim$0.6 eV shift determined here and elsewhere from XPS of single phase In_2O_3[23] and β-Ga_2O_3,[24] and perform a rigid 0.6 eV shift to the linearly extrapolated edges to higher binding energy.

Figure 5 shows the VBM to E_F separation as a function of EDX In content. Also shown are dashed lines corresponding to the In contents where phase transitions are seen. There is a slow decrease in the VBM to E_F separation from $\sim$4.3 eV on the low In(x) content end to around $\sim$4 eV In(x)$\sim$0.5, followed by a large decrease to $\sim$3.5 eV when the bixbyite phase is reached. This reflects that β-Ga_2O_3 has a much larger band gap than In_2O_3. This would indicate a valence band offset of around 0.8 eV between Ga_2O_3 and In_2O_3 with respect to E_F. Interestingly, the hexagonal (mixed) phase is much closer in energy to the monoclinic β-Ga_2O_3, possibly because its atomic coordination is closer to that of β-Ga_2O_3 than In_2O_3.
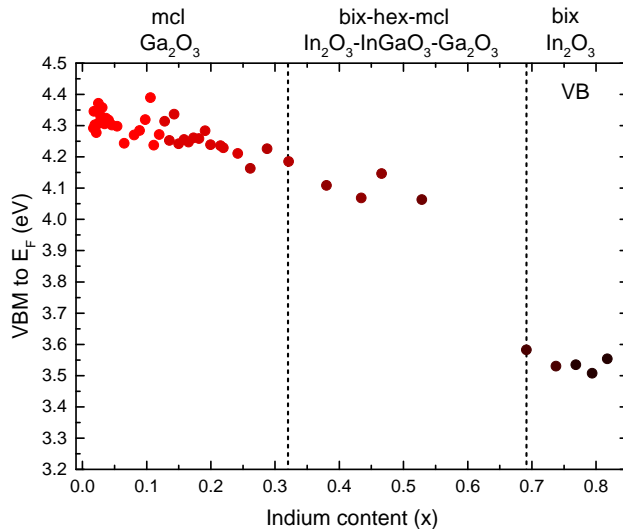
11

Figure 5: Energy positions of the VBM from XPS referenced to E_F as a function of EDX indium content. Black dashed lines separate the region of different crystallographic phase.

A similar qualitative trend in the VBM to Fermi level separation as a function of composition has very recently been reported for combinatorial $(In_xGa_{1-x})_2O_3$ films grown on both yttria-stabilized cubic zirconia and c-plane sapphire.[25] However, the values differ due to the use of raw values from linear extrapolation of the leading edge of the valence band.

3.0.3 Surface Space-Charge

The surface of In_2O_3 has previously been shown to display electron accumulation[23,26] while β-Ga_2O_3 displays electron depletion.[24,27,28] This is vital information for surface and interface sensitive devices such as chemical sensors and heterostructures. Naturally then we ask how the surface space-charge evolves over the alloy composition range, with the vision of tuning the surface electronic properties to specific device needs. To determine this, we find the barrier height Φ_B (analogous to the Schottky barrier height of a metal/semiconductor contact) which is given as the separation between the conduction band minimum (CBM) and E_F. Optical transmission measurements and derived absorption spectra (see Figure S4) were used to determine the bulk VBM to E_F separation (once the dipole forbidden transition from the topmost valence band in In_2O_3-like alloys is accounted for) at different composition points of

the material. Figure 6 displays the optical gaps extracted from transmission measurements. The intervals between measurements across the film were greater than for the XPS results, but the positions were again translated into indium content via the EDX results. Optical gaps for end-point compositions (In(x)=0 and In(x)=1) were also added to the plot from the literature.[1,24,29] An optical gap bowing curve is fitted to the data and shown in Figure 6.
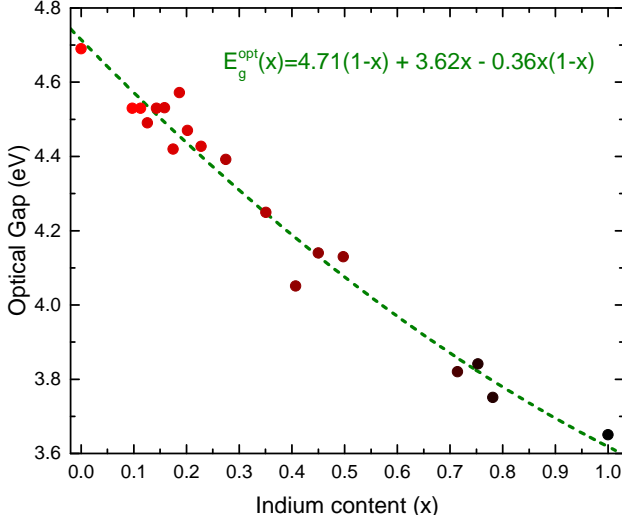

Figure 6: Optical gap versus indium content as determined via transmission spectroscopy. A fit to the data points was performed using the bowing equation,[30,31] with the fitted parameters displayed in the equation. Importantly, for x>0.6, due to transitions from the topmost valence bands being dipole forbidden, these values do not correspond to the fundamental band gap.

The optical gap bowing is described by

$$E_g^{opt}(x) = E_{Ga_2O_3}^{opt}(1-x) + E_{In_2O_3}^{opt}x - bx(1-x) \tag{1}$$

where b is the bowing parameter.[30,31] Equation 1 was used to fit the data, resulting in a bowing parameter of $b = 0.36$ eV. The optical gaps of the end-point binary compounds determined from the fit are found to be 3.62 eV for In_2O_3 and 4.71 eV for Ga_2O_3. Equation 1 is normally used to describe fundamental band gap bowing in ternary alloys where no phase change occurs, but we apply it here to the optical gaps which exhibit a smooth variation across the composition range. There is quite a wide spread of reported band gaps for Ga_2O_3

in the literature, often ranging from $\sim$4.6-4.9 eV[3] or even higher. We believe that our results are consistent with other extensive studies of the optical properties of Ga_2O_3, see for example Ref. 20. The fundamental band gap of In_2O_3 can be estimated from Figure 6 by accounting for the dipole forbidden transitions from the topmost valence bands on the In-rich side of the data set (x>0.6). The bulk VBM to E_F separation is very close to the band gap of the material, see for example Ref. 20 and the references therein, and so, we make this approximation here. This, coupled with our XPS determined surface VBM positions relative to E_F (ξ), allows us to determine $\Phi_B = E_g - \xi$. When Φ_B is positive (negative), this corresponds to the E_F lying below (above) the CBM at the surface.
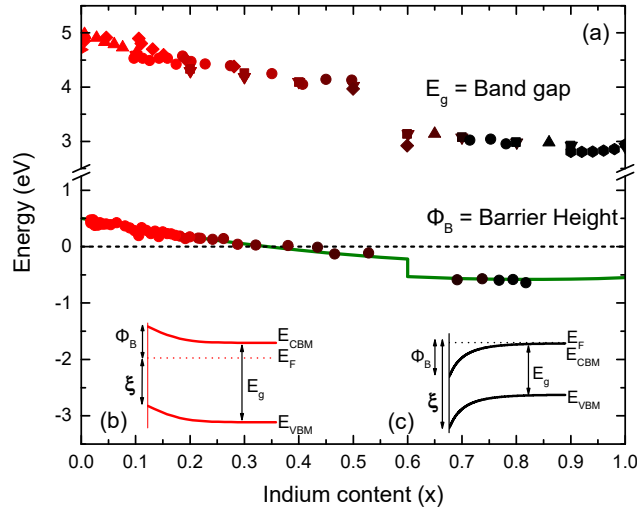

Figure 7: (a) Variation of band gap (E_g) and barrier height (Φ_B) at the $(In_xGa_{1-x})_2O_3$ surface with respect to varying indium content (x). Energy gaps were determined in this study by transmission measurements ($\bigcirc$), as well as values being taken from the literature ($\square$ Oshima,[32] $\ocircle$ Regoutz,[33] $\triangle$ Wenckstern,[34] $\triangledown$ Yang,[35] $\lozenge$ Zhang,[36] $\triangleright$ Swallow[24]). Barrier heights (Φ_B) are derived by subtracting the surface Fermi level to VBM (ξ) from the band gap (Φ_B=E_g-ξ). The surface space-charge variation is schematically represented in (b) and (c) with positive Φ_B indicating electron depletion and upward band bending (b), while negative Φ_B indicated electron accumulation and downward band bending (c).

Figure 7(a) shows E_g and Φ_B as a function of In(x) alloy composition, where E_g is accompanied by data from the literature in order to better visualise the trend.[32–36] The highest VB to lowest CB transition in In_2O_3 is known to have minimal dipole intensity,[1] and so, to achieve the real E_g value, an energy of 0.8 eV was subtracted from the measured absorp-

14

tion onsets (as this is the energy difference between the first allowed transition and dipole forbidden transitions[1]). Here, we set an In content of x = 0.6 for the phase transition from bixbyite to hexagonal (mixed) phase, as no data points exist in this region. This estimated value is informed by previous literature[31] as well as the data presented in Figures 2 and 3. The band gap smoothly decreases from ~4.7 eV at low In content, and abruptly alters when the phase changes to bixbyite before decreasing further to ~2.9 eV at high In content. Φ_B is plotted below E_g in Figure 5(a), and displays a very similar trend to the band gap. For the In-poor compositions, a positive value of Φ_B is observed corresponding to upward band bending (schematically shown in Figure 7(b)) and surface electron depletion. Φ_B then gradually decreases and is nearly zero at x = 0.35, indicating a flat bands regime with the VBM to Fermi level separation being constant as a function of depth. This then switches to downward band bending and electron accumulation in the In-rich composition range (Figure 7(c)). A guide-to-the-eye is plotted in green through Φ_B, with a discontinuity at the composition where the phase changes abruptly. In the context of electronic devices, the electron accumulation layer in bixbyite $(In_xGa_{1-x})_2O_3$ helps explain the relative difficulty in fabricating devices such as normally-off transistors and Schottky diodes[37] compared to monoclinic $(In_xGa_{1-x})_2O_3$, which displays upward band bending. Conversely, it is rather challenging to obtain ohmic contacts with low specific contact resistance with monoclinic $(In_xGa_{1-x})_2O_3$ unlike for bixbiyte $(In_xGa_{1-x})_2O_3$. Additionally, the surface electron accumulation layer of bixbiyte $(In_xGa_{1-x})_2O_3$ may also be useful for gas sensing applications,[38] whereas the surface depletion layer of monoclinic $(In_xGa_{1-x})_2O_3$ is beneficial for photo detector applications.

von Wenckstern *et al.* recently investigated the Schottky barrier characteristics of PLD combinatorial $(In_xGa_{1-x})_2O_3$ films with PtO_δ contacts via current-voltage measurements.[8] Their results are in excellent agreement with our findings, showing that the β-Ga_2O_3 phase has a higher Schottky barrier height which decreases as In content is increased. They find the barrier height difference between the two end phases to be $\Delta\Phi_{SB} \sim 0.8$ eV, reasonably

close to the difference we see here of $\Delta \Phi_B \sim 1.2$ eV. They also find that the Ga-rich phase has the best Schottky diode response (ideality factor) whilst the In-rich has the lowest series resistance. The band bending diagrams for the two binary materials are shown in Figure 7(b) and (c). Interestingly, both $In_xGa_{1-x}N$ (Ref. 39) and $In_xGa_{1-x}As$ (Refs 40,41) also display an electron accumulation to depletion transition at the surface with increasing Ga content. Those cases are simpler as no phase transition occurs across the composition range. However, the same trend is observed with Ga compounds displaying a larger band gap and higher, positive Φ_B and surface electron depletion, while In compounds have a smaller band gap with a negative Φ_B and surface electron accumulation. This will be discussed further below in the section on chemical trends.

3.0.4 Electronic Structure

To further explore the effects of the changing cation composition in $(In_xGa_{1-x})_2O_3$ alloys, we focus on the electronic structure of the stoichiometric materials In_2O_3, $InGaO_3$ and Ga_2O_3, utilizing DFT calculated DOS for the three materials. The partial and total density-of-states are displayed for Ga_2O_3, $InGaO_3$, and In_2O_3 in Figure 8(a–f). These plots show the orbital contributions (without any cross section corrections) and include a small amount of Gaussian broadening (0.1 eV full-width at half-maximum) to assist in visualizing the data. For the calculated spectra, the zero of the binding energy scale is set to the VBM.

The VBs of β-Ga_2O_3 (Figure 8(a) and (d)) and In_2O_3 (Figure 8(c) and (f)) are primarily comprised of three features. The bottom of the VB, in each case, is made up of O $2p$ mixed with Ga $4s$/In $5s$, while the middle of the VB is dominated by O $2p$, with some contribution from Ga $4p$/In $5p$ states. Finally, the top of the VB is heavily dominated by O $2p$, with a small contribution from occupied Ga $3d$/In $4d$ orbitals, indicative of p-d repulsion in these materials.[42] p-d repulsion is symmetry forbidden at Γ in octahedral symmetry complexes which forces the VBM to occur away from Γ. This effect accounts for In_2O_3 having an indirect fundamental band gap with the VBM away from the Γ-point being ~ 50 meV above
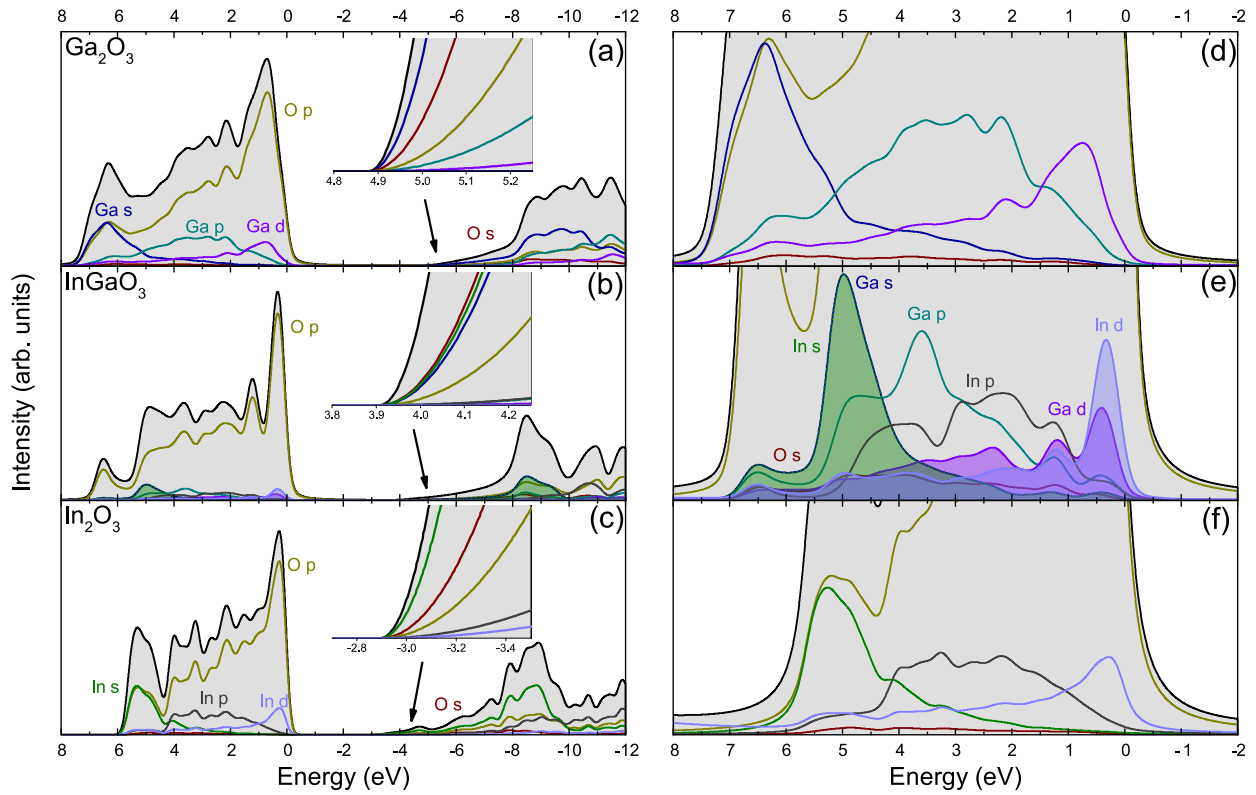
16

Figure 8: Uncorrected partial (coloured lines) and total (black lines) DOS for (a) β-Ga$_2$O$_3$, (b) hexagonal InGaO$_3$, and (c) bixbyite In$_2$O$_3$, with the insets showing an expanded region of the CBM. The valence band regions are expanded in (d)–(f). For InGaO$_3$ in (e), orbitals with strong overlap are shaded to aid in visualisation.

the highest valence band at the Γ-point.[23] Similarly, β-Ga_2O_3 has an indirect fundamental band gap of ~ 40 meV below the direct one.[43] These differences between direct and indirect band gaps are too small to be significant in most optical experiments (note that ZnO does not have octahedral symmetry and so p-d repulsion is symmetry allowed; ZnO therefore has a direct fundamental band gap at Γ.) The CBM for both β-Ga_2O_3 and In_2O_3 is dominated by Ga $4s$/In $5s$ character, with some contribution from O $2s$ (see inset in Figure 8(a-c)) as well as some from O $2p$. These are in agreement with previous calculations for In_2O_3 (Refs 1,44,45) and Ga_2O_3 (Refs 46–48).

The $InGaO_3$ structure (Figure 8(b) and (e)) has a more complex DOS than the two binary phases because it has more than two cation elemental contributions. However, many similarities can be identified. The O $2p$ component is again dominant across the whole VB. The other orbitals tend to heavily hybridize throughout the valence band structure, likely owing to the close proximity of In and Ga orbital energies. The bottom of the VB has predominantly O $2p$ orbital character ($\sim$6.5 eV). The next distinguishable feature around $\sim$5 eV is again O $2p$-dominated with strong contributions from In and Ga s states. The middle section of the DOS has additional intensity coming from Ga $4p$ and In $5p$ components which have their maximum intensity around $\sim$ 3.5 eV and $\sim$ 2 eV, respectively. These states have significant intensity over the whole VB and do not obviously mix as readily as the s and d orbitals. The VBM is again O $2p$-dominated, with contributions from In and Ga d levels. The CBM is dominated by O $2s$, In $5s$ and Ga $4s$ contributions with some O $2p$ character.

Figure 9 shows the cross-section corrected DOS (using interpolated values for 1486.6 eV from the photoionisation cross-sections tabulated in Ref. 49) including broadening by convolution with a Voigt function with $\sim$0.4 eV Gaussian and $\sim$0.3 eV Lorentzian component, compared to the experimentally determined VB spectra. The calculated and experimental VB regions are shown in Figs 9(a) and (b), respectively, while the calculated and experimental semi-core levels (Ga $3d$ and In $4d$) are shown in Figures 9(c) and (d), respectively. First, comparing Figures 9(a) and (b), we see the general features match very well throughout all
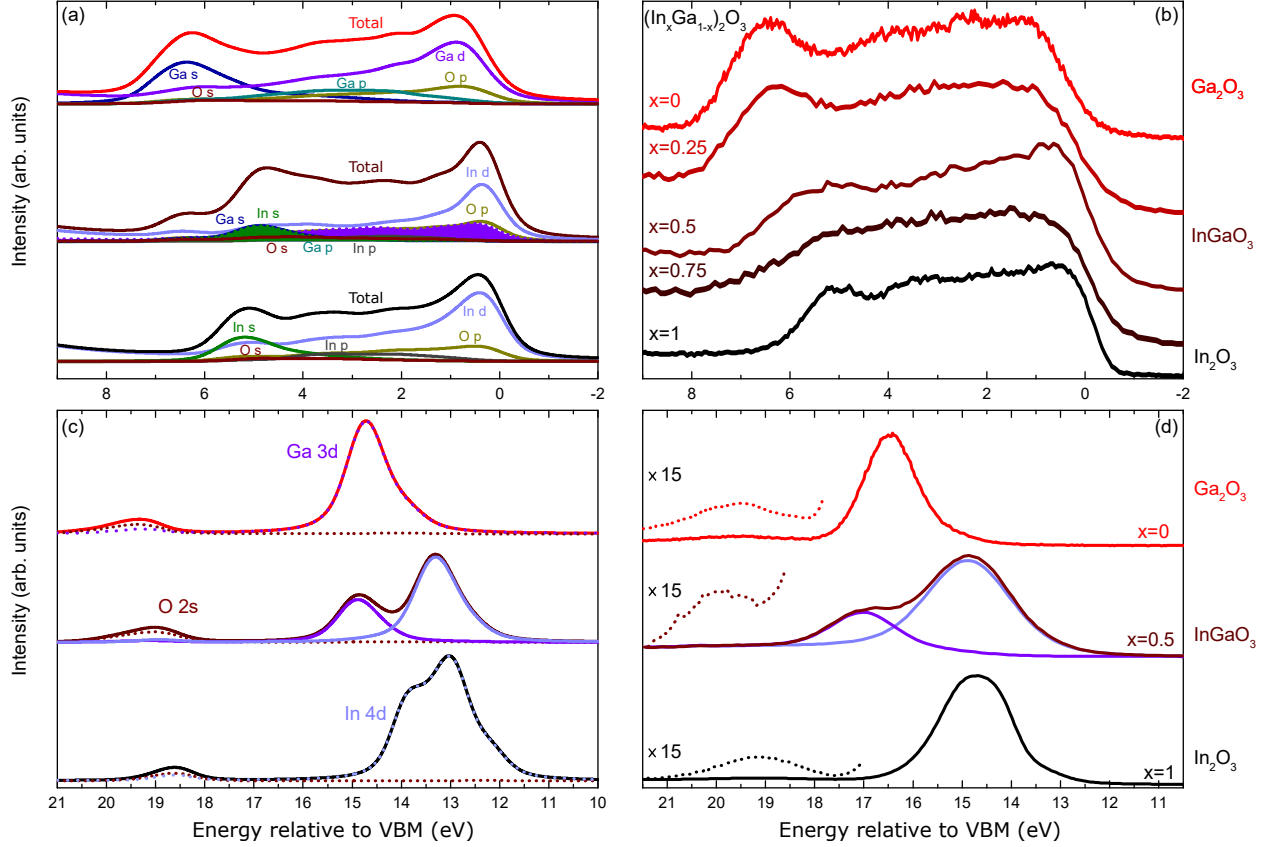
Figure 9: Valence and semi-core levels. (a) Cross-section corrected and broadened DFT partial and total VB-DOS of β-Ga$_2$O$_3$ (top), InGaO$_3$ (middle), and In$_2$O$_3$ (bottom). (b) Measured XPS VB spectra aligned to the VBM. The top and bottom spectra were taken from the Ref. 24 and 23 for single crystalline β-Ga$_2$O$_3$ (x=0) and In$_2$O$_3$ (x=1), respectively. The other spectra represent intermediate composition steps, working from top to bottom In(x) is x=0.25, x=0.5 and x=0.75, respectively. (c) DFT calculated semi core-levels for β-Ga$_2$O$_3$ (top), InGaO$_3$ (middle), and In$_2$O$_3$ (bottom). The semi core-levels are dominated by the d-orbital contributions from Ga and In. Note that SOC has been included for the In$_2$O$_3$ which splits the d band, better accounting for the broadness of the semi-core level. (d) Measured XPS semi core-level spectra of β-Ga$_2$O$_3$ (Ref. 24) (top), InGaO$_3$ (middle), and In$_2$O$_3$ (Ref. 23) (bottom). Two Gaussians are overlaid in the InGaO$_3$ spectra to aid comparison with the In $4d$ and Ga $3d$ hybrid semi-core level in the theory. The high binding energy region in each case is shown magnified $\times$15.

19

the spectra. Figure 9(a) displays the calculated β-Ga_2O_3 spectra in red, followed by the $InGaO_3$ phase in the middle in brown, and finally the In_2O_3 in black at the bottom, with the PDOS contributions labelled. Figure 9(b) shows the experimental data where the phase transition is demonstrated utilizing phase pure single crystalline data for the top and bottom spectra.[23,24] The brown spectrum in the centre belongs to the hexagonal (mixed) phase $InGaO_3$, while the spectra either side of this correspond to an In content of approximately 25% and 75%, respectively. All experimental spectra have been shifted to locate their VBM at 0 eV for comparison with the calculated DOS. Comparing the spectra in Figure 9(b), the highest binding energy feature of the β-Ga_2O_3 (Ga $4s$ dominated) is prominent around 6.5 eV, but diminishes in size and shifts to lower binding energy as In content is increased. In the $InGaO_3$ spectra, this feature is extended in energy but much less intense, matching the calculations in Figure 9(a) extremely well albeit with slightly less features resolved than calculated. This feature shifts and diminishes further, being located at $\sim$5.5 eV in pure In_2O_3. The leading edge at the VBM looks similar in the two end-point spectra, but the $InGaO_3$ phase has additional intensity due to the contribution from two cation d-levels.

Turning attention now to the calculated semi-core levels in Figure 9(c), we see both In_2O_3 and β-Ga_2O_3 have a large peak comprised nearly entirely of Ga $3d$/In $4d$ and a higher binding energy peak of mostly O $2s$ character (with some cation d mixing). The shoulder on the low binding energy side of the large peaks has a small O s contribution also, although this is swamped after cross-section corrections are applied. This s-d hybridization is associated with materials for which the cation-d and anion-s levels have similar energy.[50] Comparing the energy position of the calculated and experimental data (Figure 9(c) and (d)), we see the characteristic under-binding of these levels by the calculations,[51] especially the lower binding energy semi-core levels which are around $\sim$1-2 eV below the experimental ones.[23] This is a deficiency of the DFT approach used in these calculations,[52] despite the HSE06 functional generally giving very accurate band gaps, quasiparticle effects are neglected which have been shown to redistribute spectral weight at higher binding energies.[46,48,51] We also

see that the experimentally measured peaks are much wider than those calculated (which are broadened in the same manner as the VB in Figure 9(a)). This may be attributed to an increase in lifetime broadening for the localized semi-core levels compared with the much less localized valence states,[29] although we cannot rule out final-state relaxation effects working to narrow the valence band spectra, which are not included in the calculation.[53] Despite this, the measured regions share similar features to the calculated ones, such as the asymmetry seen in the low energy peaks. It is clear in Figure 9(d) that the In $4d$-derived peak is much wider than the Ga $3d$ peak. This is due to a higher degree of spin-orbit interaction which splits the In $4d$ band. Spin-orbit coupling (SOC) has been included in the DOS for In_2O_3 in Figure 9(c), explaining its irregular shape relative to the Ga $3d$ level in agreement with previous studies.[54] See SI Figure S6 for a comparison of the In $4d$ level calculated with and without SOC included.

The higher binding energy peaks seen around ~ 19 eV in Figure 9(c) and (d), which comprise of mostly O $2s$ character, are vastly overestimated in intensity in the calculation compared to experiment, where the intensity had to be multiplied by a factor of $\times 15$ before it was visible. This again may be attributed to the issues discussed above. The theory predicts a fairly strong contribution from the metal d-level to this peak, giving further evidence that s-d hybridization occurs in all three materials. It is also worth noting that, for the mixed phase $InGaO_3$ spectra, there are two distinct peaks around 13 and 15 eV in the theory (15 and 17 eV in the experiment). The peak intensities vary heavily with indium content (x), which is a good indicator of the extent of alloying and the stoichiometry of the system (acknowledging that the photoionisation cross section is roughly twice as large for In $4d$ compared to Ga $3d$, explaining why the In $4d$ peak is twice as intense as the Ga $3d$ peak in the stoichiometric $InGaO_3$ material).

4 Chemical Trends in Common-Cation Materials

The natural question that follows the determination of the electronic structure of a material is how does this fit with the chemical trends of related materials, such as those with a common-cation (or indeed common-anion). Here we compare the properties of In_2O_3, $InGaO_3$ and β-Ga_2O_3 with each other, and with other indium- and gallium-containing compounds in the form of the zinc-blende (ZB) and wurtzite III-V semiconductors, that have seen a lot of research in previous years.[55–57] The understanding gained from these arguably simpler systems can be used to further our understanding of the metal oxides investigated here.

Figure 10(a) shows the calculated band-edge positions for common Ga- and In-cation compounds, including In_2O_3, β-Ga_2O_3, $InGaO_3$, In-V, and Ga-V semiconductor materials with respect to the charge neutrality level (E_{CNL}). The calculated direct band gaps from the Γ-point were tuned by varying the fraction of Hartree-Fock exact exchange incorporated into HSE06 range-separated hybrid functional in order to reproduce experimental values (see for examples Refs. 1,61–63). Focusing on the VBM for the Ga-compounds in Figure 10(a) we see a general trend emerge. Firstly, the VBM are seen to increase in energy from Ga_2O_3<GaN<GaP<GaAs<GaSb with respect to E_{CNL}. As shown in Figure 8, the VBM of β-Ga_2O_3 consists of primarily O p character mixed with Ga d, while the VBM of the ZB Ga-V semiconductors are mostly of mixed anion and cation p orbital character.[56] Therefore, both sets of materials have mostly anion p orbital VBM character in common, so this is the major influence on the VBM position, and not the cation energy level. The fact that the In-compounds roughly share this VBM evolution supports this. Indeed, from Figure 10(b) of the individual elemental orbital energy levels, it is apparent that the anion p levels share exactly the same trend, increasing in energy going from O through to Sb. Also, as might be expected, $InGaO_3$ has a VBM in between that of β-Ga_2O_3 and In_2O_3. Note that the indirect transition from the VBM between Γ and M to the CBM at Γ is highlighted for $InGaO_3$, which is still between the VBM positions of β-Ga_2O_3 and In_2O_3. The only other significant indirect transition in Figure 10(a) is from GaP, where the CBM lies between Γ
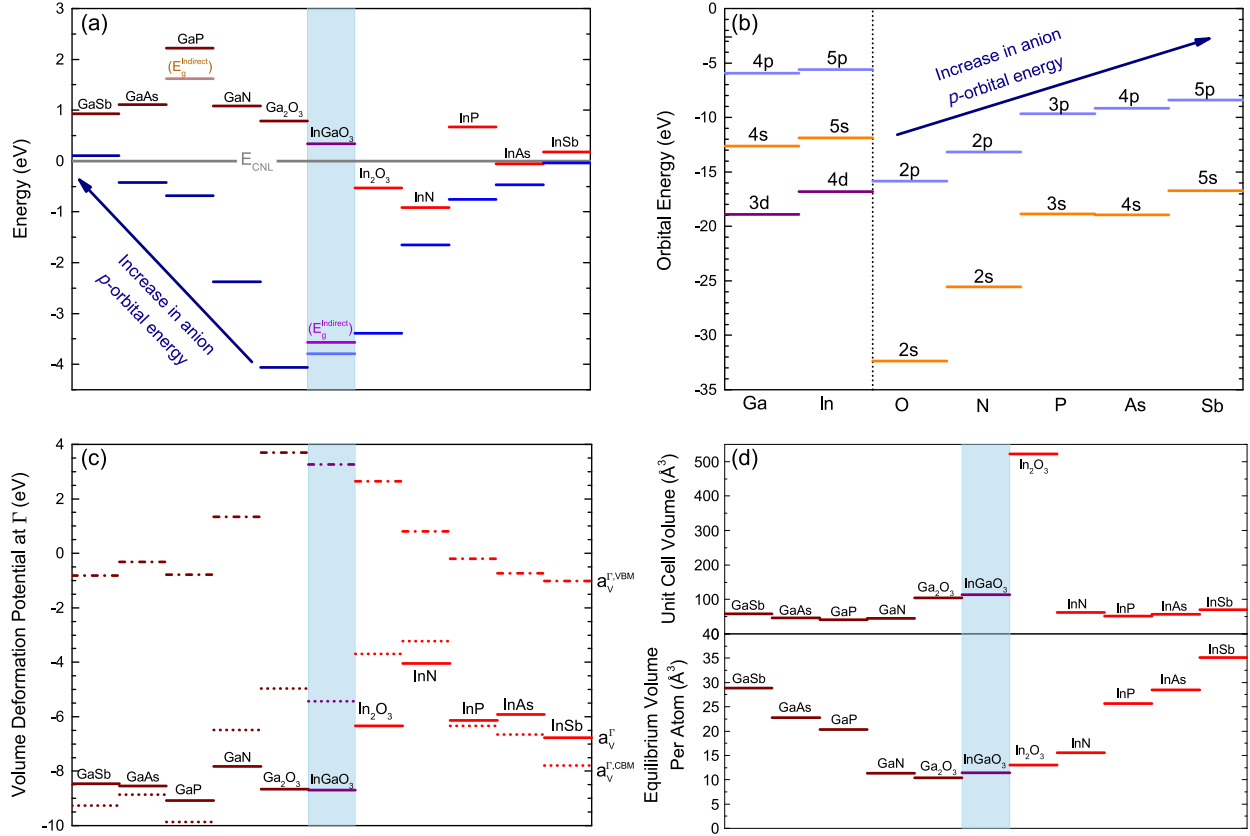
Figure 10: (a) Theoretically calculated band-edge positions for Ga and In cation compounds relative to the charge neutrality level E_{CNL}. Γ-Γ transitions are shown, but in cases where the indirect transition is significant this is indicated. (b) Atomic orbital energy levels for the constituent elements taken experimentally[58] and theoretically[59] where experiment was not available. These results corroborate the trends seen in other works.[55,60] (c) Absolute volume deformation potential at the Γ-point a_V^Γ, CBM deformation potential $a_V^{\Gamma,CBM}$, and VBM deformation potential $a_V^{\Gamma,VBM}$ for compounds. (d) Calculated equilibrium unit cell volume and volume per atom (unit cell volume normalized by the number of atoms it contains) for compounds.

and X (Ref. 61) (In_2O_3 and β-Ga_2O_3 may have a smaller indirect transition also but these may be too close to the direct band gaps to definitively prove experimentally[46,51,64]). Note also that the differences between the VBM position of the common-anion materials (see for example β-Ga_2O_3 and In_2O_3, where the VBM of β-Ga_2O_3 is lower relative to E_{CNL}) have been explained for ZB III-V and II-VI semiconductors to be due to the p-d interaction,[42,65,66] a relatively small effect in these materials compared to the orbital positioning, but explaining why the VBM of Ga-V tends to have a lower energy than In-V.

The CBM of these systems all derive from cation-anion $s - s$ hybridization. However, it is clear from Figure 10(a) and (b) that there is very little correlation between the trends of the position of the CBM and that of the individual anion/cation s levels. A useful parameter that has been used to describe the shift in band extrema with respect to an absolute energy reference (often the CNL) for crystals under volume deformation is known as the hydrostatic volume deformation potential (a_V). Hydrostatic volume deformation potentials were evaluated over a series of volumes to identify the change in the direct band gap with volume according to the formula,

$$a_V^\Gamma = \frac{dE_g^\Gamma}{dlnV} \tag{2}$$

where the direct band gap E_g^Γ was evaluated at the Γ-point from the conduction and valence band eigenvalues. While deformation potentials for relative energies, such as the band gap, are robust from first-principles calculations, changes in individual states, such as the conduction and valence band extrema, require knowledge of a suitable reference level such as a core level, vacuum level, or other state, whose dependence on volume deformations is known.[56,67–69] Cardona and Christensen[68] used Brillouin-zone averaging for deformation potentials referenced to the dielectric midgap energy, which was previously shown to be an equivalent representation of the branch-point energy (E_{BP}) and the CNL for zincblende semiconductors.[70] Following this approach, we evaluated the branch-point energies for the oxides and III-V materials with the scheme of Schleife *et al.*[71,72] using 12 valence bands and 6

conduction bands for the 10-atom monoclinic and hexagonal unit cells and 48 valence bands and 24 valence bands for the 40-atom bixbyite unit cells. With these values, we identify an E_{BP} of 4.06 eV above the VBM for Ga_2O_3 and 3.39 eV above the VBM for In_2O_3, indicating a valence band offset of 0.67 eV, in good agreement with the value $\sim$0.6 eV derived experimentally.[22,24,29] We note that the overall quantitative conclusions do depend on the choice of the numbers of bands included in the averaging,[72] but other comparable choices (e.g. 4 conduction and 8 valence bands for Ga_2O_3 and 16 conduction and 32 valence bands for In_2O_3) led to changes in the relative offsets by $\sim$0.05 eV. These values were also computed for Ga-V and In-V compounds, explicitly accounting for spin-orbit effects, with the results summarized in Table 1.

Table 1: Summary of calculated properties, including deformation potentials for the band gaps (a_V^Γ) and band edges ($a_V^{\Gamma,c}$ and $a_V^{\Gamma,v}$). The band edge deformation potentials were determined using the branch-point energy (E_{BP}, defined relative to each material's VBM) as a reference level, as described in the text. The α parameter represents the fraction of Hartree-Fock exact exchange incorporated into HSE06 range-separated hybrid functional, which was tuned to reproduce to the experimental band gaps.

	Ga_2O_3	GaN	GaP	GaAs	GaSb	In_2O_3	InN	InP	InAs	InSb	$InGaO_3$
α (%)	32	28	28	32	33	28	25	26	29	30	32
E_{BP} (eV)	4.06	2.38	0.68	0.42	-0.11	3.39	1.65	0.75	0.47	0.04	3.79
E_g^Γ (eV)	4.85	3.46	2.90	1.53	0.82	2.86	0.73	1.42	0.41	0.22	4.13
B_0 (kbar)	1844	2003	885	751	552	1715	1423	696	596	455	2026
Volume (Å^3)	104.31	45.20	40.62	45.62	57.78	522.24	62.10	51.36	56.88	70.23	113.99
V/atom (Å^3)	10.43	11.30	20.31	22.81	28.89	13.06	15.52	25.68	28.44	35.11	11.40
a_V^Γ (eV)	-8.66	-7.82	-9.08	-8.54	-8.46	-6.34	-4.04	-6.14	-5.92	-6.77	-8.70
$a_V^{\Gamma,c}$ (eV)	-4.96	-6.48	-9.86	-8.86	-9.27	-3.70	-3.23	-6.33	-6.66	-7.79	-5.43
$a_V^{\Gamma,v}$ (eV)	3.70	1.34	-0.78	-0.32	-0.81	2.64	0.81	-0.19	-0.73	-1.02	3.27

We additionally assessed the validity of E_{BP} as a suitable reference scale through tests with InP, by aligning the average electrostatic potential with the vacuum level for a series of hydrostatically strained unrelaxed, 8-layer slab models of the (111) surface. Aligned relative to the vacuum level, the deformation potentials of E_{BP} and the VBM were found to be -0.19 eV and -0.41 eV, respectively. The value for E_{BP} is on the same order as the deformation potential calculated for the VBM when aligned relative to E_{BP} ($\sim$-0.2 eV), indicating the uncertainty in this approach. This suggests that E_{BP}, similar to core levels,[69] are not fully

robust reference levels for absolute volume deformation potentials. Nonetheless, we use it to consider qualitative trends in the spirit of Cardona and Christensen. We include the calculated band gap and band edge components of the deformation potentials as a function of the equilibrium volume per atom in SI Figure S7 and S8, with the results summarized in Figure 10(c) and Table 1.

When considering the absolute deformation potentials of the band edges, as referenced to the E_{BP} in Figure 10(c), we see that $a_V^{\Gamma,v}$ (the deformation potential of the VBM) is positive for oxides and decreases as the coupling from the anion p orbitals increases, becoming negative for phosphides, arsenides and antimonides, which all share similar values. This seems to have only a small effect on the position of the VBM due to lattice compression, which is instead mostly dependent on the anion p orbital position as mentioned. $a_V^{\Gamma,c}$ tends to be a relatively large negative number, contributing much more heavily to $\mid a_V \mid$ and to the position of the CBM.[55,56,73] In this respect, we also find that the oxides do exhibit significant differences compared to the III-Vs. We find that the $a_V^{\Gamma,c}$ values are again negative for the oxides, but they exhibit a weaker dependence than that in III-Vs. We find that the conduction and valence band deformation potentials are of more comparable magnitudes in the oxides, whereas III-Vs tend to exhibit much larger magnitudes of the $a_V^{\Gamma,c}$ values relative to the $a_V^{\Gamma,v}$.

When compared to the III-Vs, we find that the oxide a_V^{Γ} (where $a_V^{\Gamma} = a_V^{\Gamma,c} - a_V^{\Gamma,v}$) values are similar, but with the nitride values deviating more than those of the oxides. Our results for the Ga-V and In-V band gap deformation potentials largely follow those in Ref. 69, exhibiting the same qualitative trends, but with slightly larger absolute values. This may be a consequence of our results being obtained with tuned hybrid functionals, as opposed to the density functional theory within the local density approximation.[69] Another apparent outlier in Figure 10(a) and (c) is InN, which was discussed previously by Wei *et al.*[55] to be in no small part due to the relatively small value of $a_V^{\Gamma,c}$ and hence small a_V^{Γ}.

Hence, the shifts in the energy gap are heavily affected not only by the positions of the

constituent orbital energy levels, but by the changes in the CBM position, the changes in a_V, and on the size of the unit cell. We plot the unit cell volumes and the volume per atom (unit cell volume divided by its occupany) in Figure 10(d) to visualise how these sizes vary between materials. Note that In_2O_3 has an extremely large unit cell, but it contains many atoms, and so its volume per atom is actually rather small in comparison to those in III-Vs. We see in Figure 10(c) that the Ga-anion semiconductors have larger $\mid a_V \mid$ than the respective In-anion semiconductors. This coupled with the fact that the Ga-based semiconductors have lower unit cell volumes than the respective indium-based compounds means Ga materials tend to have larger band gaps.

To summarise, our results are consistent with previous results on the III-V materials that identify (1) band gap deformation potentials are negative; and (2) this dependence has a far larger contribution from the deformation potential of the conduction band minima ($a_V^{\Gamma,c}$) rather than for the valence band maxima ($a_V^{\Gamma,v}$).[56,67–69] However, in contrast to the III-Vs, we find (3) larger contributions to the $a_V^{\Gamma,v}$ for the more ionic oxide semiconductors which are of comparable magnitude to the $a_V^{\Gamma,c}$.

5   Conclusion

The evolution of the electronic structure of a variable composition $(In_xGa_{1-x})_2O_3$ alloy have been determined using a combination of combinatorial XPS, measurements of the optical gap, and state-of-the-art hybrid functional DFT calculations. We show the simple trends regarding the evolution of the valence band edges in $(In_xGa_{1-x})_2O_3$. The energy of the valence band edge is reduced considerably with increasing In content when the bixbyite phase is realised. This affects the surface space-charge properties of the material. As shown, β-Ga_2O_3 displays upward surface band-bending and electron depletion, which diminishes and subsequently changes to electron accumulation with increasing In content. The bixbyite phase displays electron accumulation and downward band-bending consistent with previous

findings. The transition from accumulation to depletion for Ga-rich alloys occurs at approximately $x = 0.35$. Furthermore, we investigate the electronic structure of these materials through calculated electronic density-of-states for the phase-pure materials and compare this to XPS valence band spectra. All phases are found to have O $2p$-dominated valence bands, and have contributions from In $4d$/Ga $3d$ states at the VBM, associated with p-d repulsion. The CBM are In $5s$/Ga $4s$-dominated with a strong O $2s$ contribution. s-d hybridisation of the systems is explored looking at the semi-core levels. Finally, In_2O_3 and β-Ga_2O_3 are placed in the context of other materials in order to shed light on the origin of the optoelectronic performance of these materials, such as their wide gap nature and the n-type dopability of In_2O_3 and β-Ga_2O_3. The electronic structure and band edge positions of In_2O_3, Ga_2O_3 and $(In_xGa_{1-x})_2O_3$ alloys have been understood in terms of their place within chemical trends of common-cation and common-anion materials. Trends in atomic orbital energies have been examined and deformation potentials have been calculated. Compared with III-V semiconductors, it was found that there is a larger contribution to the a_V^{Γ} values from the $a_V^{\Gamma,v}$ terms for the more ionic oxide semiconductors which are of comparable magnitude to the $a_V^{\Gamma,c}$ terms. The volume deformation potentials are -8.66 eV for Ga_2O_3, -8.70 eV for $InGaO_3$ and -6.34 eV for In_2O_3.

Acknowledgement

Supporting Information Available

XPS core levels and associated analysis, optical transmission and absorption spectra, XPS semi-core levels, DFT of semi-core levels accounting for SOC, DFT calculated band gap deformation potentials.

This material is available free of charge via the Internet at `http://pubs.acs.org/`.

References

(1) Walsh, A.; Silva, J. L. F. D.; Wei, S.-H.; Körber, C.; Klein, A.; Piper, L. F. J.; DeMasi, A.; Smith, K. E.; Panaccione, G.; Torelli, P.; Payne, D. J.; Bourlange, A.; Egdell, R. G. Nature of the Band Gap of In_2O_3 Revealed by First-Principles Calculations and X-Ray Spectroscopy. *Physical Review Letters* **2008**, *100*, 167402.

(2) Ellmer, K. Past Achievements and Future Challenges in the Development of Optically Transparent Electrodes. *Nature Photonics* **2012**, *6*, 809–817.

(3) Pearton, S. J.; Yang, J.; Cary, P. H.; Ren, F.; Kim, J.; Tadjer, M. J.; Mastro, M. A. A Review of Ga_2O_3 Materials, Processing, and Devices. *Applied Physics Reviews* **2018**, *5*, 011301.

(4) Lorenz, M. et al. The 2016 Oxide Electronic Materials and Oxide Interfaces Roadmap. *Journal of Physics D: Applied Physics* **2016**, *49*, 433001.

(5) Gonalves, G.; Barquinha, P.; Pereira, L.; Franco, N.; Alves, E.; Martins, R.; For-

tunato, E. High Mobility a-IGO Films Produced at Room Temperature and Their Application in TFTs. *Electrochemical and Solid State Letters* **2010**, *13*, H20–H22.

(6) Huang, W.-L.; Hsu, M.-H.; Chang, S.-P.; Chang, S.-J.; Chiou, Y.-Z. Indium Gallium Oxide Thin Film Transistor for Two-Stage UV Sensor Application. *ECS Journal of Solid State Science and Technology* **2019**, *8*, Q3140–Q3143.

(7) Kim, Y. G.; Kim, T.; Avis, C.; Lee, S.-H.; Jang, J. Stable and High-Performance Indium Oxide Thin-Film Transistor by Ga Doping. *IEEE Transactions on Electron Devices* **2016**, *63*, 1078–1084.

(8) von Wenckstern, H.; Splith, D.; Werner, A.; Müller, S.; Lorenz, M.; Grundmann, M. Properties of Schottky Barrier Diodes on $(In_xGa_{1-x})_2O_3$ for $0.01 \leq x \leq 0.85$ Determined by a Combinatorial Approach. *ACS Combinatorial Science* **2015**, *17*, 710–715.

(9) Kranert, C.; Lenzner, J.; Jenderka, M.; Lorenz, M.; von Wenckstern, H.; Schmidt-Grund, R.; Grundmann, M. Lattice Parameters and Raman-active Phonon Modes of $(In_xGa_{1-x})_2O_3$ for $x < 0.4$. *Journal of Applied Physics* **2014**, *116*, 013505.

(10) Shannon, R. D.; Preqitt, C. T. Synthesis and Structure of Phases in the In_2O_3-Ga_2O_3 System. *Journal of Inorganic and Nuclear Chemistry* **1968**, *30*, 1389–1398.

(11) Kneiß, M.; Hassa, A.; Splith, D.; Sturm, C.; von Wenckstern, H.; Lorenz, M.; Grundmann, M. Epitaxial Stabilization of Single Phase κ-$(In_xGa_{1x})_2O_3$ Thin Films up to x = 0.28 on c-Sapphire and κ-Ga_2O_3(001) Templates by Tin-Assisted VCCS-PLD. *APL Materials* **2019**, *7*, 101102.

(12) Heyd, J.; Scuseria, G. E.; Ernzerhof, M. Hybrid Functionals Based on a Screened Coulomb Potential. *The Journal of Chemical Physics* **2003**, *118*, 8207–8215.

(13) Blöchl, P. E. Projector Augmented-Wave Method. *Physical Review B* **1994**, *50*, 17953–17979.

(14) Kresse, G.; Furthmüller, J. Efficient Iterative Schemes for Ab Initio Total-energy Calculations using a Plane-wave Basis Set. *Physical Review B* **1996**, *54*, 11169–11186.

(15) Blöchl, P. E.; Jepsen, O.; Andersen, O. K. Improved Tetrahedron Method for Brillouin-zone Integrations. *Physical Review B* **1994**, *49*, 16223–16233.

(16) Onuma, T.; Saito, S.; Sasaki, K.; Goto, K.; Masui, T.; Yamaguchi, T.; Honda, T.; Kuramata, A.; Higashiwaki, M. Temperature-Dependent Exciton Resonance Energies and their Correlation with IR-active Optical Phonon Modes in β-Ga_2O_3 Single Crystals. *Applied Physics Letters* **2016**, *108*, 101904.

(17) Ingebrigtsen, M. E.; Varley, J. B.; Kuznetsov, A. Y.; Svensson, B. G.; Alfieri, G.; Mihaila, A.; Badstbner, U.; Vines, L. Iron and Intrinsic Deep Level States in Ga_2O_3. *Applied Physics Letters* **2018**, *112*, 042104.

(18) Geller, S. Crystal Structure of β-Ga_2O_3. *The Journal of Chemical Physics* **1960**, *33*, 676–684.

(19) Prozheeva, V.; Hölldobler, R.; von Wenckstern, H.; Grundmann, M.; Tuomisto, F. Effects of Alloy Composition and Si-doping on Vacancy Defect Formation in $(In_xGa_{1-x})_2O_3$ Thin Films. *Journal of Applied Physics* **2018**, *123*, 125705.

(20) Schmidt-Grund, R.; Kranert, C.; Böntgen, T.; von Wenckstern, H.; Krau, H.; Grundmann, M. Dielectric Function in the NIR-VUV Spectral Range of $(In_xGa_{1-x})_2O_3$ Thin Films. *Journal of Applied Physics* **2014**, *116*, 053510.

(21) von Wenckstern, H.; Kneiß, M.; Hassa, A.; Storm, P.; Splith, D.; Grundmann, M. A Review of the Segmented-Target Approach to Combinatorial Material Synthesis by Pulsed-Laser Deposition. *physica status solidi (b)* **2020**, *257*, 1900626.

(22) Vines, L.; Bhoodoo, C.; von Wenckstern, H.; Grundmann, M. Electrical Conductivity of In_2O_3 and Ga_2O_3 after Low Temperature Ion Irradiation; Implications for Intrinsic

Defect Formation and Charge Neutrality Level. *Journal of Physics: Condensed Matter* **2018**, *30*, 025502.

(23) King, P. D. C.; Veal, T. D.; Fuchs, F.; Wang, C. Y.; Payne, D. J.; Bourlange, A.; Zhang, H.; Bell, G. R.; Cimalla, V.; Ambacher, O.; Egdell, R. G.; Bechstedt, F.; McConville, C. F. Band Gap, Electronic Structure, and Surface Electron Accumulation of Cubic and Rhombohedral In_2O_3. *Physical Review B* **2009**, *79*, 205211.

(24) Swallow, J. E. N.; Varley, J. B.; Jones, L. A. H.; Gibbon, J. T.; Piper, L. F. J.; Dhanak, V. R.; Veal, T. D. Transition from Electron Accumulation to Depletion at β-Ga_2O_3 Surfaces: The Role of Hydrogen and the Charge Neutrality Level. *APL Materials* **2019**, *7*, 022528.

(25) Nagata, T.; Hoga, T.; Yamashita, A.; Asahi, T.; Yagyu, S.; Chikyow, T. Valence Band Modification of a $(Ga_xIn_{1x})_2O_3$ Solid Solution System Fabricated by Combinatorial Synthesis. *ACS Combinatorial Science* **2020**, *22*, 433439.

(26) King, P. D. C.; Veal, T. D.; Payne, D. J.; Bourlange, A.; Egdell, R. G.; McConville, C. F. Surface Electron Accumulation and the Charge Neutrality Level in In_2O_3. *Physical Review Letters* **2008**, *101*, 116808.

(27) Lovejoy, T. C.; Chen, R.; Zheng, X.; Villora, E. G.; Shimamura, K.; Yoshikawa, H.; Yamashita, Y.; Ueda, S.; Kobayashi, K.; Dunham, S. T.; Ohuchi, F. S.; Olmstead, M. A. Band Bending and Surface Defects in β-Ga_2O_3. *Applied Physical Letters* **2012**, *100*, 181602.

(28) Navarro-Quezada, A.; Alamé, S.; Esser, N.; Furthmüller, J.; Bechstedt, F.; Galazka, Z.; Skuridina, D.; Vogt, P. Near Valence-band Electronic Properties of Semiconducting β-Ga_2O_3 (100) Single Crystals. *Physical Review B* **2015**, *92*, 195306.

(29) King, P. D. C.; Veal, T. D.; Schleife, A.; Zúñiga-Pérez, J.; Martel, B.; Jefferson, P. H.; Fuchs, F.; Muñoz-Sanjosé, V.; Bechstedt, F.; McConville, C. F. Valence-band Electronic

Structure of CdO, ZnO, and MgO from X-ray Photoemission Spectroscopy and Quasi-particle-corrected Density-functional Theory Calculations. *Physical Review B* **2009**, *79*, 205205.

(30) Moses, P. G.; Van de Walle, C. G. Band Bowing and Band Alignment in InGaN Alloys. *Applied Physics Letters* **2010**, *96*, 021908.

(31) Peelaers, H.; Steiauf, D.; Varley, J. B.; Janotti, A.; Van de Walle, C. G. $(In_xGa_{1-x})_2O_3$ Alloys for Transparent Electronics. *Physical Review B* **2015**, *92*, 085206.

(32) Oshima, T.; Fujita, S. Properties of Ga_2O_3-based $(In_xGa_{1-x})_2O_3$ Alloy Thin Films Grown by Molecular Beam Epitaxy. *Physica Status Solidi (C)* **2008**, *5*, 3113–3115.

(33) Regoutz, A.; Egdell, R.; Morgan, D.; Palgrave, R.; Téllez, H.; Skinner, S.; Payne, D.; Watson, G.; Scanlon, D. Electronic and Surface Properties of Ga-doped In_2O_3 Ceramics. *Applied Surface Science* **2014**, *349*, 970–982.

(34) von Wenckstern, H.; Splith, D.; Purfürst, M.; Zhang, Z.; Kranert, C.; Müller, S.; Lorenz, M.; Grundmann, M. Structural and Optical Properties of $(In,Ga)_2O_3$ Thin Films and Characteristics of Schottky Contacts Thereon. *Semiconductor Science and Technology* **2015**, *30*, 024005.

(35) Yang, F.; Ma, J.; Luan, C.; Kong, L. Structural and Optical Properties of $Ga_{2(1-x)}In_{2x}O_3$ films Prepared on α-Al_2O_3 (0001) by MOCVD. *Applied Surface Science* **2009**, *255*, 4401–4404.

(36) Zhang, Z.; von Wenckstern, H.; Lenzner, J.; Lorenz, M.; Grundmann, M. Visible-blind and Solar-blind Ultraviolet Photodiodes Based on $(In_xGa_{1-x})_2O_3$. *Applied Physics Letters* **2016**, *108*, 123503.

(37) Michel, J.; Splith, D.; Rombach, J.; Papadogianni, A.; Berthold, T.; Krischok, S.; Grundmann, M.; Bierwagen, O.; von Wenckstern, H.; Himmerlich, M. Processing

Strategies for High-Performance Schottky Contacts on n-Type Oxide Semiconductors: Insights from In_2O_3. *ACS Applied Materials and Interfaces* **2019**, *11*, 27073–27087.

(38) Rombach, J.; Papadogianni, A.; Mischo, M.; Cimalla, V.; Kirste, L.; Ambacher, O.; Berthold, T.; Krischok, S.; Himmerlich, M.; Selve, S.; Bierwagen, O. The Role of Surface Electron Accumulation and Bulk Doping for Gas-Sensing Explored with Single-Crystalline In_2O_3 Thin Films. *Sensors and Actuators B: Chemical* **2016**, *236*, 909 – 916.

(39) Veal, T. D.; Jefferson, P. H.; Piper, L. F. J.; McConville, C. F.; Joyce, T. B.; Chalker, P. R.; Considine, L.; Lu, H.; Schaff, W. J. Transition from Electron Accumulation to Depletion at InGaN Surfaces. *Applied Physics Letters* **2006**, *89*, 202110.

(40) Kajiyama, K.; Mizushima, Y.; Sakata, S. Schottky Barrier Height of n-$In_xGa_{1-x}As$ Diodes. *Applied Physics Letters* **1973**, *23*, 458.

(41) Lüth, H. Research on III-V Semiconductor Interfaces: Its Impact on Technology and Devices. *Physica Status Solidi (a)* **2001**, *187*, 33–44.

(42) Wei, S.-H.; Zunger, A. Role of Metal d States in II-VI Semiconductors. *Physical Review B* **1988**, *37*, 8958.

(43) Varley, J. B.; Weber, J. R.; Janotti, A.; Van de Walle, C. G. Oxygen Vacancies and Donor Impurities in β-Ga_2O_3. *Applied Physics Letters* **2010**, *97*, 142106.

(44) Karazhanov, S. Z.; Ravindran, P.; Vajeeston, P.; Ulyashin, A.; Finstad, T. G.; Fjellvåg, H. Phase Stability, Electronic Structure, and Optical Properties of Indium Oxide Polytypes. *Physical Review B* **2007**, *76*, 075129.

(45) Mryasov, O. N.; Freeman, A. J. Electronic Band Structure of Indium Tin Oxide and Criteria for Transparent Conducting Behavior. *Physical Review B* **2001**, *64*, 233111.

(46) Furthmüller, J.; Bechstedt, F. Quasiparticle Bands and Spectra of Ga_2O_3 Polymorphs. *Physical Review B* **2016**, *93*, 115204.

(47) Hajnal, Z.; Miró, J.; Kiss, G.; Réti, F.; Deák, P.; Herndon, R. C.; Kuperberg, J. M. Role of Oxygen Vacancy Defect States in the n-type Conduction of β-Ga_2O_3. *Journal of Applied Physics* **1999**, *86*, 3792.

(48) Swallow, J. E. N. et al. Influence of Polymorphism on the Electronic Structure of Ga_2O_3. *Chem. Mater.* **2020**, *32*, 8460–8470.

(49) Scofield, J. *Theoretical photoionization cross sections from 1 to 1500 keV.*; 1973.

(50) Persson, C.; Zunger, A. s-d Coupling in Zinc-blende Semiconductors. *Physical Review B* **2003**, *68*, 073205.

(51) Fuchs, F.; Bechstedt, F. Indium-oxide Polymorphs from First Principles: Quasiparticle Electronic States. *Physical Review B* **2008**, *77*, 155107.

(52) Fuchs, F.; Furthmüller, J.; Bechstedt, F. Quasiparticle Band Structure based on a Generalized Kohn-Sham Scheme. *Physical Review B* **2007**, *76*, 115109.

(53) Ley, L.; Pollak, R. A.; McFeely, F. R.; Kowalczyk, S. P.; Shirley, D. A. Total Valence-band Densities of States of III-V and II-VI Compounds from X-ray Photoemission Spectroscopy. *Physical Review B* **1974**, *9*, 600–621.

(54) Erhart, P.; Klein, A.; Egdell, R. G.; Albe, K. Band Structure of Indium Oxide: Indirect Versus Direct Band Gap. *Physical Review B* **2007**, *75*, 153205.

(55) Wei, S.-H.; Nie, X.; Batyrev, I. G.; Zhang, S. B. Breakdown of the Band-gap-common-cation Rule: The Origin of the Small Band Gap of InN. *Physical Review B* **2003**, *67*, 165209.

(56) Wei, S.-H.; Zunger, A. Predicted Band-gap Pressure Coefficients of all Diamond and Zinc-blende Semiconductors: Chemical Trends. *Physical Review B* **1999**, *60*, 5404.

(57) Li, Y.-H.; Gong, X. G.; Wei, S.-H. Ab Initio All-Electron Calculation of Absolute Volume Deformation Potentials of IV-IV, III-V, and II-VI Semiconductors: The Chemical Trends. *Physical Review B* **2006**, *73*, 245206.

(58) Mann, J. B.; Meek, T. L.; Allen, L. C. Configuration Energies of the Main Group Elements. *Journal of the American Chemical Society* **2000**, *122*, 2780–2783.

(59) Fischer, C. F. Average-energy-of-configuration Hartree-Fock Results for the Atoms Helium to Radon. *Atomic Data and Nuclear Data Tables* **1973**, *12*, 87–99.

(60) Herman, F.; Skillman, S. *Atomic Structure Calculations*; Prentice-Hall: Englewood Cliffs, NJ, 1963.

(61) Vurgaftman, I.; Meyer, J. R.; Ram-Mohan, L. R. Band Parameters for III-V Compound Semiconductors and their Alloys. *Journal of Applied Physics* **2001**, *89*, 5815–5875.

(62) Wu, J.; Walukiewicz, W.; Shan, W.; Yu, K. M.; Ager, J. W.; Li, S. X.; Haller, E. E.; Lu, H.; Schaff, W. J. Temperature Dependence of the Fundamental Band Gap of InN. *Journal of Applied Physics* **2003**, *94*, 4457–4460.

(63) Tippins, H. H. Optical Absorption and Photoconductivity in the Band Edge of β-Ga$_2$O$_3$. *Physical Review* **1965**, *140*, A316–A319.

(64) Varley, J. B.; Schleife, A. Bethe–Salpeter Calculation of Optical-absorption Spectra of In$_2$O$_3$ and Ga$_2$O$_3$. *Semiconductor Science and Technology* **2015**, *30*, 024010.

(65) Wei, S.-H.; Zunger, A. Calculated Natural Band Offsets of all II-VI and III-V Semiconductors: Chemical Trends and the Role of Cation d Orbitals. *Applied Physics Letters* **1998**, *72*, 2011.

(66) Wei, S.-H.; Zunger, A. Role of d Orbitals in Valence-Band Offsets of Common-Anion Semiconductors. *Physical Review Letters* **1987**, *59*, 144.

(67) Van de Walle, C. G.; Martin, R. M. "Absolute" Deformation Potentials: Formulation and Ab initio Calculations for Semiconductors. *Physical Review Letters* **1989**, *62*, 2028–2031.

(68) Cardona, M.; Christensen, N. E. Acoustic Deformation Potentials and Heterostructure Band Offsets in Semiconductors. *Physical Review B* **1987**, *35*, 6182–6194.

(69) Li, Y.-H.; Gong, X. G.; Wei, S.-H. Ab initio All-electron Calculation of Absolute Volume Deformation Potentials of IV-IV, III-V, and II-VI Semiconductors: The Chemical Trends. *Physical Review B* **2006**, *73*, 245206.

(70) Varley, J. B.; Samanta, A.; Lordi, V. Descriptor-Based Approach for the Prediction of Cation Vacancy Formation Energies and Transition Levels. *Journal of Physical Chemistry Letters* **2017**, *8*, 5059–5063.

(71) Schleife, A.; Fuchs, F.; Rödl, C.; Furthmüller, J.; Bechstedt, F. Branch-point Energies and Band Discontinuities of III-nitrides and III-/II-oxides from Quasiparticle Bandstructure Calculations. *Applied Physics Letters* **2009**, *94*, 012104.

(72) Shapera, E. P.; Schleife, A. Database-Driven Materials Selection for Semiconductor Heterojunction Design. *Advanced Theory and Simulations* **2018**, *1*, 1800075.

(73) Walsh, A.; Catlow, C. R. A.; Zhang, K. H. L.; Egdell, R. G. Control of the Band-gap States of Metal Oxides by the Application of Epitaxial Strain: The Case of Indium Oxide. *Physical Review B* **2011**, *83*, 161202(R).

Graphical TOC Entry